Mesoscale Updraft Magnitude and Cloud-Ice Content Deduced from the Ice Budget of the Stratiform Region of a Tropical Cloud Cluster[1]

DEAN D. CHURCHILL AND ROBERT A. HOUZE, JR.

Department of Atmospheric Sciences, University of Washington, Seattle, WA 98195

(Manuscript received 27 June 1983, in final form 2 March 1984)

ABSTRACT

Radar observations obtained during Winter MONEX describe the three-dimensional structure and development of the mesoscale stratiform region of a tropical cloud cluster. The magnitudes of the mesoscale updraft and cloud-ice mass content within an upper tropospheric stratiform cloud deck are deduced from a formulation of the ice budget of the stratiform region. Measurements of radar reflectivity at upper levels serve as the primary input data. Aircraft observations of ice particles are also used to guide the calculations. The mesoscale updraft magnitude and cloud-ice mass content are determined hourly over a period of 12 h. The updraft velocities were 10–23 cm s^{-1}, and the cloud-ice contents were 0.1–0.3 g m^{-3}. The vertical velocity estimates agree well with estimates obtained for the same cloud cluster by Johnson (1982) using the kinematic method.

1. Introduction

Recent studies have determined the magnitude of the vertical air motion in mesoscale updrafts and downdrafts located in the stratiform regions of tropical cloud clusters (Gamache and Houze, 1982; Johnson, 1982; Houze and Rappaport, 1984). These studies have inferred vertical motions kinematically from rawinsonde data. In this paper we use a different approach, based on radar measurements and airborne cloud microphysical observations, to deduce mesoscale updraft magnitudes in the stratiform region of a tropical cloud cluster.

The cloud cluster used for this purpose was observed during the Global Atmospheric Research Programme's Winter Monsoon Experiment (WMONEX). It is the "cluster B" described by Churchill and Houze (1984), who used data from a radar sited at Bintulu on the north coast of Borneo to describe the development of this cluster. Using gridded reflectivity data, with horizontal resolution of 4 km and vertical resolution of 2 km, they applied an objective technique to distinguish between the convective and stratiform regions of the cluster. From aircraft observations, they deduced that ice particles sampled at about the 8 km level in the stratiform region of cluster B had grown in water-saturated conditions consistent with the presence of a mesoscale updraft. Johnson (1982) determined the magnitude of this mesoscale upper-tropospheric stratiform updraft by kinematic analysis of sounding data obtained from WMONEX ships located in the vicinity of cluster B. (Comparison of Fig. 1 of Johnson, 1982, with the satellite images in Fig. 5 of Churchill and Houze, 1984, shows that the same cluster was examined in both papers.) In this paper, we determine the magnitude of the mesoscale updraft at upper levels in the stratiform region of cluster B by using radar reflectivity and cloud microphysical observations in an analysis of the ice budget of the stratiform cloud deck. The cloud-ice mass content needed to balance the ice budget is determined simultaneously.

Section 2 derives the ice budget of the stratiform precipitation region, Section 3 describes the input obtained from microphysical and radar observations, and Section 4 presents the results of calculations of updraft magnitude and cloud-ice content.

2. Ice budget of the upper-level stratiform deck

a. Formulation and simplifying assumptions

Churchill and Houze (1984) used an objective technique (referred to as "partitioning") to distinguish the stratiform precipitation of cluster B from its convective precipitation. An ice budget is now formulated for the objectively determined stratiform region, and the area-averaged (or "mesoscale") updraft and the area-averaged cloud-ice content needed to balance the budget are deduced. The budget calculations will be applied at the 9 km level, which is the height at which Johnson (1982) found the updraft to be at a maximum.

A scheme of the type devised by Kessler (1969) is used, except that here it is applied to cloud ice and precipitation ice rather than cloud liquid water and rain. The term *precipitation ice* refers to all frozen hydrometeors with diameters greater than 500 μm,

[1] Contribution No. 679, Department of Atmospheric Sciences, University of Washington.

while *cloud ice* refers to smaller frozen hydrometeors. The threshold of 500 μm was used by Rutledge and Hobbs (1983) to distinguish between cloud and precipitation ice. The substantial derivatives of precipitation ice content I_p and cloud-ice content I_c, in mass per unit volume, are related to source, sink and conversion terms:

$$\frac{dI_c}{dt} = -A - C + G, \tag{1}$$

$$\frac{dI_p}{dt} = A + C + F, \tag{2}$$

where A is autoconversion from cloud to precipitation ice, C is collection of cloud ice by precipitation ice, G is generation of cloud ice, F (defined more precisely below) is the flux convergence of I_p due to precipitation fallspeeds, and t is time. Adding Eqs. (1) and (2) gives

$$\frac{d}{dt}(I_c + I_p) = G + F. \tag{3}$$

The term F is computed as the net convergence of precipitation falling into and out of a 2 km deep layer that is centered at an altitude of 9 km. It is expressed by

$$F = \rho g \frac{\partial}{\partial p}(\hat{v}_f I_p), \tag{4}$$

where ρ is the density of the air (considered to be only a function of pressure p), g the acceleration of gravity, and $\hat{v}_f$ (a negative quantity) is a fallspeed assumed to apply to all the precipitation ice comprising I_p. The choice of a value for $\hat{v}_f$ is somewhat arbitrary. Kessler (1969) used the median-diameter fall velocity. Here we follow Atlas *et al.* (1973) and let $\hat{v}_f$ be the radar-reflectivity-weighted mean fall velocity. Full discussion of $\hat{v}_f$ can be found in Section 3 and Appendix B.

The source term G in Eq. (3) is assumed to be the rate at which water vapor is condensed as a result of upward motion. This is approximated by

$$G = -\omega \frac{\partial}{\partial p}(\rho q_s), \tag{5}$$

where ω is the vertical velocity of the air in pressure coordinates and q_s is the saturation mixing ratio with respect to liquid water. The vertical derivative is assumed to be constant in time. Expanding the time derivative in (3) and substituting from Eqs. (4) and (5) gives

$$\frac{\partial}{\partial t}(I_c + I_p) + \mathbf{V}\cdot\nabla(I_c + I_p) + \omega \frac{\partial}{\partial p}(I_c + I_p) = -\omega \frac{\partial}{\partial p}(\rho q_s) + \rho g \frac{\partial}{\partial p}(\hat{v}_f I_p), \tag{6}$$

where $\mathbf{V}$ is the horizontal wind velocity.

b. Determination of mesoscale vertical motion

To determine the mesoscale updraft velocity, Eq. (6) is averaged over the area of the stratiform region and simplified. The areal average of an arbitrary quantity f is defined as

$$\bar{f} = \sigma^{-1} \int_\sigma f d\sigma, \tag{7}$$

where the overbar denotes averaging over the area σ covered by the stratiform precipitation region. Because the area increases and decreases during the cluster's life cycle, σ is treated as a function of time. Applying Eq. (7) to (6) gives

$$\overline{\frac{\partial}{\partial t}(I_c + I_p)} + \overline{\mathbf{V}\cdot\nabla(I_c + I_p)} + \overline{\omega \frac{\partial}{\partial p}(I_c + I_p)} + \overline{\omega \frac{\partial}{\partial p}(\rho q_s)} = \overline{\rho g \frac{\partial}{\partial p}(\hat{v}_f I_p)}. \tag{8}$$

It is shown in Appendix A that

$$\overline{\frac{\partial I_p}{\partial t}} = \frac{\partial \bar{I}_p}{\partial t} + (\bar{I}_p - \tilde{I}_p)\frac{\partial}{\partial t}(\ln\sigma), \tag{9a}$$

$$\overline{\frac{\partial I_c}{\partial t}} = \frac{\partial \bar{I}_c}{\partial t} + (\bar{I}_c - \tilde{I}_c)\frac{\partial}{\partial t}(\ln\sigma), \tag{9b}$$

where the tilde represents an average taken around the boundary of the precipitation area.

Assumptions must be made about the values of $\tilde{I}_c$ and $\tilde{I}_p$. Along the outer boundaries of the stratiform precipitation area σ, the radar reflectivity and hence I_p, fall to very low levels. Additional boundaries occur along the edges of convective cells embedded in σ. Examples of the distribution of convective regions within the stratiform area of cluster B can be seen in the reflectivity patterns shown in Fig. 18 of Churchill and Houze (1984). Values of $\tilde{I}_p$ were obtained by averaging the values of I_p indicated by radar reflectivity observations along the boundaries of σ. Since the precipitation area σ is embedded in a widespread cloud, we assume that the cloud-ice content I_c does not change abruptly at the edge of σ. For simplicity, we assume that the value of I_c on the boundary of σ is the same as the average value of I_c within σ; thus, we set

$$\tilde{I}_c = \bar{I}_c. \tag{10}$$

To test the sensitivity of the results to this assumption, we have also set $\tilde{I}_c$ to zero in one case, and to $10\bar{I}_c$ in another. The resulting values of $\bar{\omega}$ and $\bar{I}_c$ changed by less than 0.3%. The third left-hand term of (8) is written as

$$\overline{\omega \frac{\partial}{\partial p}(I_c + I_p)} = \bar{\omega}\,\overline{\frac{\partial}{\partial p}(I_c + I_p)}. \tag{11}$$

We have assumed that in a deep stratiform cloud, the vertical eddy fluxes of I_p and I_c are negligible compared to the mean flux. Using (A10) and (10), we may rewrite (11) as

$$\overline{\bar{\omega}\frac{\partial}{\partial p}(I_c + I_p)} = \bar{\omega}\left[\frac{\partial}{\partial p}(\bar{I}_c + \bar{I}_p) + (\bar{I}_p - \tilde{I}_p)\frac{\partial \ln\sigma}{\partial p}\right]. \tag{12}$$

The vertical gradient of $\bar{I}_c$ is assumed to be comparable at most to that of $\bar{I}_p$. It will be seen that this latter gradient is much smaller than $\partial(\rho q_s)/\partial p$, hence no large error could be introduced by omitting $\partial\bar{I}_c/\partial p$ from Eq. (12). Employing (9a)–(12), recalling that $\partial(\rho q_s)/\partial p$ has been assumed constant, and ignoring vertical advection of I_c, we may rewrite (8) as

$$\frac{\partial}{\partial t}(\bar{I}_c + \bar{I}_p) + (\bar{I}_p - \tilde{I}_p)\frac{\partial \ln\sigma}{\partial t} + \overline{\mathbf{V}\cdot\nabla(I_p + I_c)} + \bar{\omega}\left[\frac{\partial \bar{I}_p}{\partial p} + (\bar{I}_p - \tilde{I}_p)\frac{\partial \ln\sigma}{\partial p} + \frac{\partial}{\partial p}(\rho q_s)\right] = \rho g\overline{\frac{\partial}{\partial p}(\hat{v}_f I_p)}. \tag{13}$$

Solving for $\bar{\omega}$ yields an expression for the mesoscale vertical motion:

$$\bar{\omega} = -\left[\underbrace{-\rho g\overline{\frac{\partial}{\partial p}(\hat{v}_f I_p)}}_{\text{Precipitation fallspeed flux convergence (Term 1)}} + \underbrace{\frac{\partial}{\partial t}(\bar{I}_c + \bar{I}_p)}_{\text{Storage (Term 2)}} + \underbrace{(\bar{I}_p - \tilde{I}_p)\frac{\partial \ln\sigma}{\partial t}}_{\text{Area tendency (Term 3)}} + \underbrace{\overline{\mathbf{V}\cdot\nabla(I_p + I_c)}}_{\text{Horizontal advection (Term 4)}}\right]\left[\underbrace{\frac{\partial \bar{I}_p}{\partial p} + (\bar{I}_p - \tilde{I}_p)\frac{\partial \ln\sigma}{\partial p}}_{\text{Vertical gradient of precipitation-ice content (Term 5)}} + \underbrace{\frac{\partial}{\partial p}(\rho q_s)}_{\text{Condensation (Term 6)}}\right]^{-1}. \tag{14}$$

Eq. (14) expresses the magnitude of the vertical motion needed to provide sufficient condensation (Term 6) and vertical transport of ice (Term 5) to balance the precipitation fallspeed flux convergence (Term 1), plus the time rates of change of cloud and precipitation ice content due to storage (Term 2), change in the size of the stratiform area (Term 3), and net horizontal advection of hydrometeors (Term 4). Evaluations of the terms in (14) are presented in Section 3.

c. *Determination of cloud-ice mass content*

The diagnostic equation for $\bar{I}_c$ is based on Eq. (2). The autoconversion and collection terms in (2) are parameterized as in Rutledge and Hobbs (1983). Autoconversion is expressed by

$$\bar{A} = \begin{cases} \dfrac{\bar{I}_c - I_{c\max}}{\delta}, & \bar{I}_c > I_{c\max} \\ 0, & \bar{I}_c \leq I_{c\max}, \end{cases} \tag{15}$$

where $I_{c\max} = 0.339$ g m^{-3} and $\delta = 10$ s. Collection is expressed as

$$\bar{C} = \bar{I}_c C^*, \tag{16}$$

$$C^* = \frac{\pi}{4} a E_{SI} N_0 \left(\frac{\rho_0}{\rho}\right)^{0.4} \frac{\Gamma(b+3)}{\lambda_s^{b+3}}. \tag{17}$$

We used a value of 0.1 for the collection efficiency E_{SI}, as did Rutledge and Hobbs (1983) (however, the sensitivity of the results to the assumed value was tested and is discussed in Section 4); N_0 (given in Table 1) is the intercept of the Marshall–Palmer size distribution assumed to apply to the precipitation particles at 9 km, ρ_0 and ρ are air density at the surface and 9 km, respectively, a and b are empirical constants relating fallspeed to particle size (see Section 3d), and Γ is the gamma function. The parameter λ_s is the slope of the Marshall–Palmer distribution and is given by

$$\lambda_s = (\pi \rho_s N_0/\bar{I}_p)^{0.25}, \tag{18}$$

where ρ_s is the density of the ice particles. We used a value of $\rho_s = 100$ kg m^{-3}, which was used by Rutledge and Hobbs (1983) for regions of mesoscale lifting with weak vertical air motions (0.1–0.2 m s^{-1}). The sensitivity of results to the assumed density of the ice particles is discussed in Section 4.

The diagnostic equation for $\bar{I}_c$ is obtained from Eq. (2) by expanding the time derivative, substituting for F from (4), averaging over area, ignoring vertical eddy fluxes, and using (9a). The result is

TABLE 1. Thermodynamic and microphysical parameters. Temperature T and pressure p were obtained from the Winter MONEX mean ship sounding. N_0 (m^{-4}) was obtained as a function of T from the results of Houze *et al.* (1979).

z (km)	p (mb)	T (°C)	ρ (kg m^{-3})	$(\rho_0/\rho)^{0.4}$	N_0 (m^{-4})
11	225	−45	0.344	1.651	1.6×10^8
9	308	−29	0.471	1.472	5.0×10^7
7	410	−14	0.552	1.281	1.3×10^7

$$\frac{\partial \bar{I}_p}{\partial t} + (\bar{I}_p - \tilde{I}_p)\frac{\partial \ln\sigma}{\partial t} + \bar{\omega}\frac{\partial \bar{I}_p}{\partial p} + \bar{\omega}(\bar{I}_p - \tilde{I}_p)\frac{\partial \ln\sigma}{\partial p} + \overline{\mathbf{V}\cdot\nabla I_p} - \rho g\overline{\frac{\partial}{\partial p}(\hat{v}_f I_p)} = \bar{A} + \bar{C}. \quad (19)$$

Since, according to (15) and (16), $A + C$ is a function of $\bar{I}_c$ and $\bar{I}_p$, and $\bar{I}_p$ is determined from radar observations, Eqs. (14) and (19) form a pair of simultaneous equations in the two unknowns $\bar{\omega}$ and $\bar{I}_c$. We solved the two equations numerically for each time period by initially guessing $\bar{I}_c$ to be zero and obtaining a first estimate of $\bar{\omega}$ from Eq. (14). The value of $\bar{\omega}$ was then used in Eq. (19) to obtain an estimate of $\bar{I}_c$. The $\bar{I}_c$ estimate then was inserted in Eq. (14) to obtain a revised estimate of $\bar{\omega}$. Further revisions were made until the estimates of $\bar{\omega}$ and $\bar{I}_c$ changed by less than 1% from one iteration to the next. We assumed $\partial\bar{I}_c/\partial t$ was zero at the first time period, and employed a backward step at subsequent time periods.

3. Analysis of radar data

The primary input to the model is the equivalent radar reflectivity factor Z_e from the MIT WR-73 radar at Bintulu. The data are stored on tape in decibels of Z_e (dBZ_e). In the discussion below, the variable E is used to represent values of dBZ_e. Since the 9 km level of cluster B was well above the 0°C level, the E values were converted to values of radar reflectivity factor for ice scatterers, Z_i, according to the relation

$$Z_i(E) = 4.68 \times 10^{E/10}. \quad (20)$$

In this expression, the factor 4.68 is the square of the ratio of the magnitudes of the complex indices of refraction of ice and water (Battan, 1973, p. 38 onward).

a. Determination of precipitation ice content

Values of precipitation ice content I_p (kg m^{-3}) were determined from the Z_i values (mm^6 m^{-3}) by the relation

$$I_p(Z_i) = 8.0 \times 10^{-6} Z_i^{0.61} \quad (21)$$

(Herzegh and Hobbs, 1980). Area averages of I_p were determined by obtaining a frequency distribution of

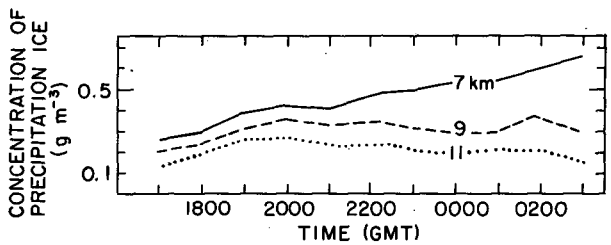

FIG. 1. Area-averaged radar-detected concentrations of precipitation ice (I_p) at the 7, 9 and 11 km levels of the stratiform region of cluster B during 9 and 10 December 1978.

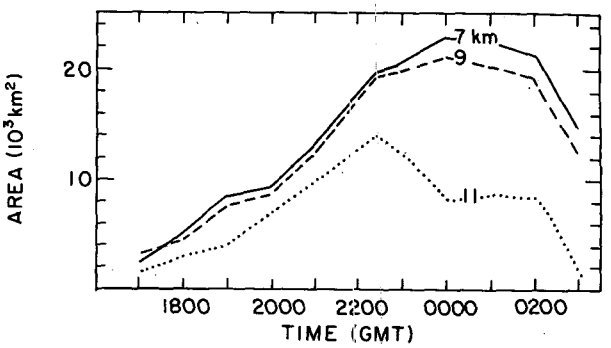

FIG. 2. Area covered by stratiform precipitation at the 7, 9 and 11 km levels of the stratiform region of cluster B during 9 and 10 December 1978.

E-values, $f(E_j)$, where E_j are integral values ranging from 1 to 63, and obtaining a weighted average of I_p values throughout the stratiform echo according to

$$\bar{I}_p = \{\sum_j f(E_j) I_p[Z_i(E_j)]\}[\sum_j f(E_j)]^{-1}. \quad (22)$$

If I_p is thought of as an arbitrary variable, Eq. (22) represents the general formula for determining area-averaged quantities used in this study.

The observed $\bar{I}_p$ values for 11 times, spaced about 1 h apart during the lifetime of the stratiform region of cluster B, are shown in Fig. 1. At 7 km, $\bar{I}_p$ increased from 0.26 to 0.65 g m^{-3} over the period shown. The 9 km $\bar{I}_p$ values increased less, from 0.2 to 0.3 g m^{-3}, and the 11-km level values increased least, from 0.14 to 0.15 g m^{-3}. These values of $\bar{I}_p$ were used in Eqs. (14) and (19). Centered differences were used for all derivatives in this study, except for $\partial\bar{I}_c/\partial t$ which was approximated by a backward difference.

b. Area covered by stratiform precipitation

The partitioning method of Churchill and Houze (1984) was used to identify the regions of convective precipitation in the 10 December 1978 cloud cluster (see their Fig. 18). The regions of echo not identified as convective were classified as stratiform. Figure 2 shows the time variation of the area classified as stratiform at 7, 9 and 11 km. The 11 km area, which reached its peak at 2200 GMT, was apparently associated with detrainment of hydrometeors from the tops of nearby convective cells, which were most numerous in the cluster at about 2300 GMT 9 December 1978 (Fig. 19a of Churchill and Houze, 1984). The peak areas at 7 and 9 km occurred at 0000 GMT 10 December and covered a much larger area than at 11 km. This time corresponds to the mature stage of the stratiform cloud deck, and we associate the relatively large area at 7 and 9 km with the development of the upper-tropospheric mesoscale updraft within the stratiform region of the cluster. The 7, 9 and 11 km areas were used to determine the factor $\partial(\ln\sigma)/\partial p$ in Eqs. (14) and (17).

c. Advection

Advection of I_p and I_c was estimated in two ways. The first method, which we call the "Gamache and Houze" scheme, assumes the horizontal advection of $(I_p + I_c)$ was proportional to the condensation rate within the stratiform precipitation region. This parameterization is motivated by the results of Gamache and Houze (1983), who determined, in the case of a GATE squall line with trailing stratiform region, that about 1.4 times as much water was advected from the convective line into the stratiform region than was produced as condensate by the mesoscale updraft. [From Fig. 12 of Gamache and Houze (1983) it can be seen that the ratio C_A/C_{mu}, where C_A is the total condensate (cloud plus precipitation) transported horizontally into the stratiform region and C_{mu} is the total water condensed within the stratiform region by the mesoscale updraft, was estimated to lie between 1.2 and 1.7. We have taken the average of these two empirical estimates (1.4) to estimate the ratio of the horizontal advection to the condensation term in Eq. (14).] Term (4) of Eq. (14) becomes

$$\overline{\bar{\mathbf{V}} \cdot \nabla(I_c + I_p)} = 1.4\bar{\omega} \frac{\partial}{\partial p} (\rho q_s). \tag{23}$$

Then, solving Eq. (14) for $\bar{\omega}$, we obtain

$$\bar{\omega} = \frac{\overline{-\rho g \partial/\partial p(\hat{v}_f I_p)} + \partial/\partial t(\bar{I}_c + \bar{I}_p) + (\bar{I}_p - \hat{I}_p)\partial \ln\sigma/\partial t}{\partial \bar{I}_p/\partial p + (\bar{I}_p - \hat{I}_p)\partial \ln\sigma/\partial p + 2.4\partial/\partial p(\rho q_s)}. \tag{24}$$

Physically, this equation states that under these conditions the advection of hydrometeors from the convective cells into the stratiform region reduces the magnitude of the updraft needed to balance the water budget of the stratiform region. This scheme is an extreme case relative to cluster B, because this cluster does not have the solid line of convection on the windward side as did the squall line of Gamache and Houze (1983). Therefore, this method produces a lower limit on the magnitude of $\bar{\omega}$.

Our second advection scheme, which we call the "precipitation-only" scheme, is formulated by first expressing the advection as the sum of mean and eddy components:

$$\overline{\bar{\mathbf{V}} \cdot \nabla(I_c + I_p)} = \bar{\mathbf{V}} \cdot \overline{\nabla(I_c + I_p)} + \overline{\mathbf{V}' \cdot \nabla'(I_p + I_c)}. \tag{25}$$

We have no information on eddy components of the wind, and no observational information on advection of cloud ice I_c, so we dropped these terms. However, the radar data give values of I_p, so this term may be retained. By using a mean easterly (x-direction) wind $\bar{u}$ of 10 m s^{-1}, constant in time (see Fig. 4 of Churchill and Houze, 1984, for the synoptic setting), we then estimated the mean advection of I_p according to

$$\bar{\mathbf{V}} \cdot \overline{\nabla(I_c + I_p)} = \bar{u}\, \overline{\partial I_p/\partial x}. \tag{26}$$

The derivative $\partial I_p/\partial x$ was determined by obtaining area averages of centered differences of I_p from the radar reflectivity patterns at 9 km. This method produces an upper limit on the magnitude of $\bar{\omega}$ by underestimating the magnitude of the advection, thereby requiring a stronger updraft to provide more condensate to balance the budget. The results of the two methods are presented in Section 4.

d. Determination of particle fallspeeds

It is shown in Appendix B that for a given reflectivity value Z_i and height z, the reflectivity-weighted fallspeed $\hat{v}_f$ is

$$\hat{v}_f(Z_i, z) = -a \frac{\Gamma(7 + b)}{\Gamma(7)} \left[\frac{Z_i}{\Gamma(7)N_0(z)}\right]^{b/7} \left[\frac{\rho_0}{\rho(z)}\right]^{0.4}, \tag{27}$$

where $\rho(z)$ is the air density at height z.

In situ observations of ice particles during the decaying stage of cluster B were described by Churchill and Houze (1984). Particles were predominantly irregular in shape, suggesting that most were aggregates, and sharp edges indicated a lack of riming. Identifiable habits included columns and branched crystals, the latter having the appearance of sideplanes. Accordingly, we have chosen values of $a = 1.88$ and $b = 0.12$, which correspond to unrimed aggregates of sideplanes (Hobbs, 1974, p. 673). Values of a and b for other types of unrimed or lightly rimed aggregates do not change our results significantly. Area-averaged values of $\hat{v}_f$ are shown in Fig. 3 at 7, 9 and 11 km altitudes. The fallspeeds were nearly steady state at all altitudes, indicating that weak change in terminal fallspeed occurred throughout the period. The fallspeeds increased with height from about 1.1 m s^{-1} at 7 km to 1.4 m s^{-1} at 11 km. This gradient is due primarily to the density factor in (27); at higher altitudes, rarified air permits higher fallspeeds.

e. Determination of precipitation rate

Precipitation rates were determined by multiplying particle fallspeeds by the radar-detected ice content,

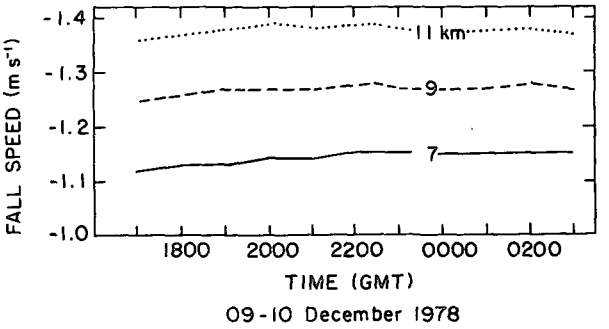

FIG. 3. Area-averaged, Z-weighted fallspeeds of precipitation ice at the 7, 9 and 11 km levels of the stratiform region of cluster B during 9 and 10 December 1978.

discussed in Section 3a above, then averaging over the area to obtain values of $\overline{\hat{v}_f I_p}$. These are shown in Fig. 4, expressed in units of mm h^{-1}. At all times, the precipitation rate decreased with height. At 11 km, relative maxima occurred at 2000 and 0100 GMT, corresponding respectively to the period of intense convection and the mature stage of the stratiform cloud deck. The precipitation rate at 7 km increased throughout the period except for a relative minimum at 2100 GMT. The wide separation between the 7 and 9 km levels after 2200 GMT indicates that the mesoscale updraft was enhancing the difference in precipitation rates between the two levels. Using these data, we evaluated Term 1 of Eq. (14) according to

$$\overline{\frac{\partial}{\partial p}(\hat{v}_f I_p)} = \frac{\partial}{\partial p}\overline{\hat{v}_f I_p} + (\overline{\hat{v}_f I_p} - \widetilde{\hat{v}_f I_p})\frac{\partial \ln\sigma}{\partial p}, \quad (28)$$

as in Eq. (A10).

f. Other data

Table 1 lists the values of pressure, temperature, density and N_0 needed to complete the evaluation of the terms in Eq. (14). Term 6 in (14) (assumed to be constant in time) was evaluated from the sounding data shown in Table 1.

4. Results

a. Updraft magnitude

The terms in the numerator of the right side of Eq. (14) are shown in Fig. 5a as functions of time. These are the time rates of change associated with the precipitation fallspeed flux convergence (Term 1), storage of precipitation ice (Term 2), and the rate of change of area of precipitation (Term 3). The horizontal advection (Term 4) is the "precipitation-only" estimate,

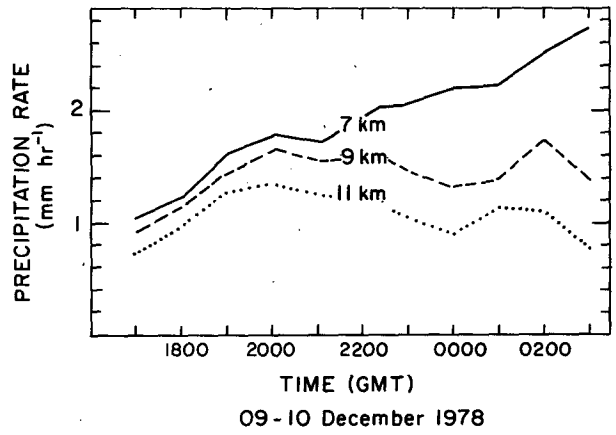

FIG. 4. Area-averaged precipitation rates at the 7, 9 and 11 km levels of the stratiform region of cluster B during 9 and 10 December 1978.

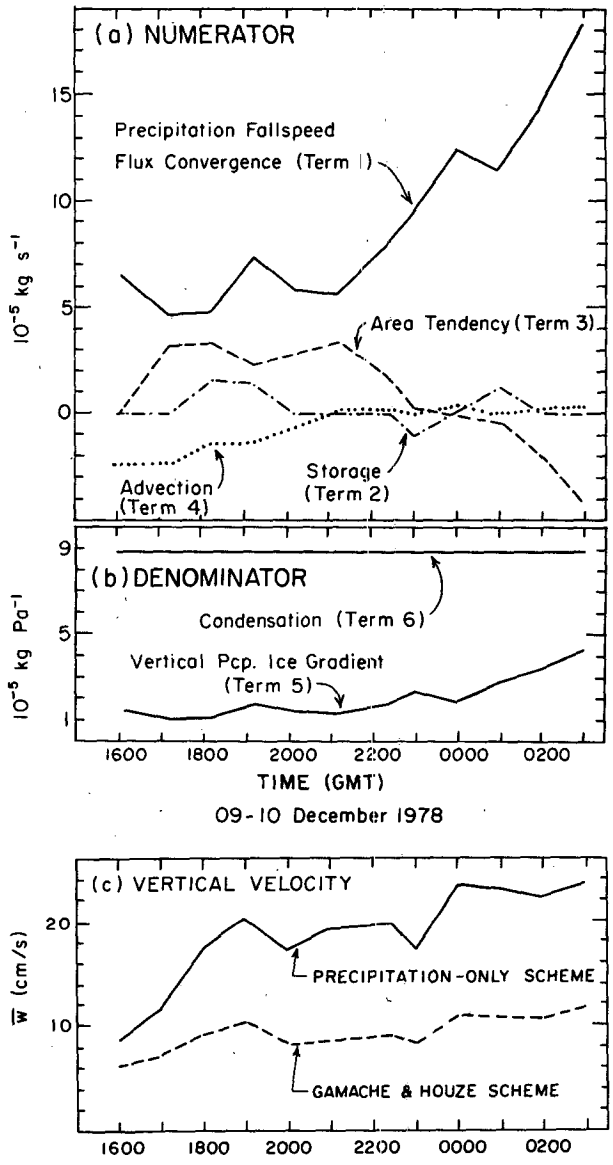

FIG. 5. Component terms and magnitude of mesoscale updraft. (a) Values of the terms in the numerator of Eq. (14). (b) Values of the two terms in the denominator of Eq. (14). (c) Magnitude of the mesoscale updraft; the "precipitation-only" scheme (solid line) assumed that only precipitation ice was advected into the cloud deck by an easterly wind of 10 m s^{-1}; The "Gamache and Houze" scheme parameterized advection of hydrometeors as proportional to the condensation rate in the cloud deck.

computed according to (26). The characteristics of these curves are consistent with the life cycle of the cluster. The developing stages of the cluster (from 1600 to 2300 GMT) are characterized by an expanding area of stratiform precipitation (positive values of Term 3), with positive storage of precipitation ice (positive values of Term 2), advection of precipitation ice from nearby convective cells into the stratiform region (negative values of Term 4), and a relatively steady rate of pre-

cipitation fallspeed flux convergence (Term 1) into the layer of air centered on 9 km.

The mature stage of the cluster, from 2300 GMT onward, was characterized by a decreasing area of stratiform precipitation, negligible advection of precipitation and storage, and a rapidly increasing precipitation fallspeed flux convergence, which can be explained by the presence and strengthening of a mesoscale updraft that generated much condensation within the 2 km layer.

The denominator terms of Eq. (14) are shown in Fig. 5b. The top horizontal line represents the assumed-constant value of the vertical gradient of saturation mixing ratio, which by means of updraft motion generates condensation that produces cloud ice. This value is much greater than the vertical gradient of precipitation-ice content (lower curve) even though the latter increases with time. Thus the upward transport of precipitation ice at 9 km by the updraft motion is significantly less than the generation of ice through condensation associated with the updraft.

The mesoscale updraft velocity in height coordinates is obtained by dividing $\bar{\omega}$ by $-\rho g$. The velocity obtained by the "precipitation-only" estimate of hydrometeor advection (Section 3c) is indicated by the solid curve in Fig. 5c and represents an upper limit. The updraft magnitude generally increased with time from 1600 to 1900 GMT, reaching 22 cm s^{-1}, decreased to an average of about 19 cm s^{-1} through 2300 GMT, then increased to about 23 cm s^{-1} from 0000 to 0300 GMT. The dashed curve indicates the updraft obtained using the "Gamache and Houze" advection scheme. These values were about half the magnitude of the mean-advection values and represent a lower limit. These values of $\bar{\omega}$ agree well with updraft velocity estimates of 6–10 cm s^{-1} deduced by Johnson (1982) from Winter MONEX ship rawinsondes and aircraft dropwindsondes. The cloud-area vertical velocities that he diagnosed were for the same cloud cluster studied here, but he used a mutually exclusive data set and different physical principles. Thus we conclude that the good agreement between Johnson's results and our results reinforces the credibility of both techniques and the results of both studies.

The apparently decreasing area of precipitation after 0100 GMT (term 3, Fig. 5a) may have been at least partly due to the precipitation moving out of radar range, rather than dissipating. If so, the increasing precipitation fallspeed flux convergence during the period 0100–0300 GMT indicates that the magnitude of the updraft was still increasing even though our calculations show that the updraft magnitude was nearly steady state through this period.

The updraft velocities were very insensitive to the assumed values of ice density and collection efficiency, and to the value of the cloud-ice content itself. The cloud-ice content, however, was very sensitive to the ice density and collection efficiency, as discussed below.

b. Cloud-ice mass contents

Cloud-ice-mass content was obtained by solving Eq. (19) for $\bar{I}_c$, and the results are shown in Fig. 6. Using both advection schemes with a collection efficiency of 0.1 and an ice density of 100 kg m^{-3}, the values of ice content increased from ~0.1 to 0.3 g m^{-3} during the period studied. Changes in values from one scheme to the other were of order 10%. Also shown in Fig. 6 are values computed using the "precipitation-only" scheme, but with different values of the collection efficiency and ice density. Increasing the collection efficiency by an order of magnitude decreased the ice contents by the same (dashed curve). The dot-dashed curve shows that doubling the ice density increased the ice content by roughly 50%.

5. Conclusions

Analysis of the ice budget of the stratiform cloud deck of a winter monsoon cloud cluster was accomplished by use of conventional land-based radar data and airborne cloud microphysical observations. The magnitude of the mesoscale updraft within the upper-level deck was deduced as the vertical motion needed to supply sufficient condensation and upward transport of precipitation ice to balance the ice budget of a 2 km thick layer of air centered on 9 km altitude. The updraft began during the cloud cluster's intensifying stage (as defined by Leary and Houze, 1979, and de-

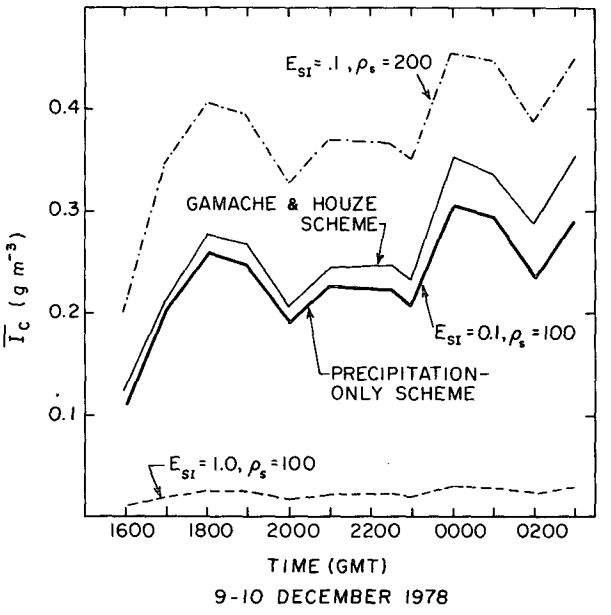

FIG. 6. Magnitude of cloud-ice mass content. The bold solid line shows the ice content using the "precipitation-only" scheme, while the thin solid line is for the "Gamache and Houze" advection scheme. Both use a collection efficiency E_{SI} of 0.1, with ice density ρ_s 100 kg m^{-3}. The dashed curve shows the "precipitation-only" scheme, using E_{SI} = 1.0 and ρ_s = 100, and the dash-dot curve shows the same with E_{SI} = 0.1 and ρ_s = 200.

scribed for this cluster by Churchill and Houze, 1984) and attained a maximum value of 10–23 cm s^{-1} during the mature stage of the cluster. Area-averaged cloud-ice mass contents were also determined from the ice budget. Cloud-ice content ranged from 0.1 to 0.3 g m^{-3}.

The updraft velocity magnitude was sensitive to the vertical distribution of area-averaged precipitation rate in the stratiform cloud deck. Because the precipitation rates were determined by empirical relationships between radar reflectivity and ice mass content, and ice particle size and fallspeed, it is difficult to state quantitatively what uncertainty resulted. The updraft magnitudes were insensitive to the choice of collection efficiency and ice density. Values of cloud ice content, however, were sensitive to the magnitude of the updraft and the assumed values of ice density and collection efficiency. The updraft speeds agreed well with the results of Johnson (1982), who used a kinematic method and different physical principles to obtain vertical motions from soundings obtained in the vicinity of the same cluster that we have studied. This agreement lends credibility to the two techniques. Neither study, however, addresses the dynamics whereby the mesoscale updraft was initiated, and this remains a topic for further research.

Acknowledgments. We wish to thank E. J. Zipser, S. A. Rutledge, and S. K. Esbensen for their valuable comments on this work. S. G. Geotis and R. H. Johnson provided data for the study, C. Arthur typed the text and K. Moore drafted the figures. This research was sponsored by the National Science Foundation under Grant ATM80-17327.

APPENDIX A

Area-Averaged Derivatives

1. Time derivatives

Given an area $\sigma(t)$ with length $L(t)$ around a border that moves in the direction of the border's normal vector at speed $u_n(t, \theta)$, where θ is the angular coordinate in a polar frame, an analytical expression for the area-averaged time rate of change of a quantity in this area can be obtained.

For an arbitrary quantity f, we define the area average as

$$\bar{f} = \sigma^{-1} \int_\sigma f d\sigma. \tag{A1}$$

The deviation from this mean is

$$f' = f - \bar{f}. \tag{A2}$$

The average taken around the border is defined as

$$\tilde{f} = \frac{1}{L} \oint f dl, \tag{A3}$$

and the deviation from the border average is

$$f'' = f - \tilde{f}. \tag{A4}$$

By taking the local time derivative of f, we obtain

$$\frac{\partial \bar{f}}{\partial t} = \sigma^{-1} \left(\frac{\partial}{\partial t} \int_\sigma f d\sigma - \bar{f} \frac{\partial \sigma}{\partial t} \right). \tag{A5}$$

Using polar coordinates and applying Leibnitz' rule for differentiation of an integral with variable limits, we may express the first term in the parentheses as

$$\frac{\partial}{\partial t} \int_\sigma f d\sigma = \int_\sigma \frac{\partial f}{\partial t} d\sigma + \int_0^{2\pi} f(R) R \frac{\partial R}{\partial t} d\theta, \tag{A6}$$

where $f(R)$ is the value of f along the boundary of the region, and R is the distance from the origin to a point on the boundary. The speed of movement of the boundary normal to itself is $u_n = \partial R/\partial t$. Since $f = \tilde{f} + f''$, $u_n = \tilde{u}_n + u_n''$, and $dl = Rd\theta$, the rightmost integral of Eq. (A6) may be written as

$$\int_0^{2\pi} f(R) R \frac{\partial R}{\partial t} d\theta = \oint f u_n dl = L(\tilde{f}\tilde{u}_n + \widetilde{f''u_n''}). \tag{A7}$$

In this study we assumed that there were no correlations between f and u_n along the boundary, so we omitted the eddy term in Eq. (A7). Since

$$\tilde{u}_n = L^{-1} \oint u_n dl = L^{-1} \frac{\partial \sigma}{\partial t}, \tag{A8}$$

substituting Eqs. (A6)–(A8) in (A5) yields

$$\overline{\frac{\partial f}{\partial t}} = \frac{\partial \bar{f}}{\partial t} + (\bar{f} - \tilde{f}) \frac{\partial \ln \sigma}{\partial t}. \tag{A9}$$

The rightmost term can be interpreted as an "entrainment" factor: As the domain changes size, the area average changes if the average value of f along the boundary differs from the interior average.

2. Pressure derivative

A similar analysis can be carried out for derivatives with respect to pressure. Replacement of time t in Eq. (A9) with pressure p yields

$$\overline{\frac{\partial f}{\partial p}} = \frac{\partial \bar{f}}{\partial p} + (\bar{f} - \tilde{f}) \frac{\partial \ln \sigma}{\partial p}. \tag{A10}$$

APPENDIX B

Reflectivity-Weighted Fallspeeds

Locatelli and Hobbs (1974) showed that the fallspeed v_f of an ice particle varies with its maximum diameter D according to

$$v_f(D) = aD^b, \tag{B1}$$

where a and b are constants for a given particle type. Following Atlas *et al.* (1973), we define a reflectivity-weighted fallspeed $\hat{v}_f$ as

$$\hat{v}_f = \frac{-\int_0^\infty v_f(D)dZ_i}{\int_0^\infty dZ_i}, \quad \text{(B2)}$$

where $dZ = N(D)D^6dD$, $N(D)$ is the number of ice particles in the size range D to $D + dD$, and the minus sign is included to make $\hat{v}_f$ negative since it represents downward motion. Assuming that $N(D)$ has the form of a Marshall–Palmer distribution,

$$N(D) = N_0 e^{-\lambda_s D}, \quad \text{(B3)}$$

and carrying out the integration indicated in (B2), we obtain

$$\hat{v}_f = \frac{-a\Gamma(7 + b)}{\lambda_s{}^b\Gamma(7)}. \quad \text{(B4)}$$

Since

$$Z_i = \int_0^\infty N_0 \exp(-\lambda_s D)D^6 dD, \quad \text{(B5)}$$

it follows that

$$\lambda_s = \{[N_0\Gamma(7)]/Z_i\}^{1/7}, \quad \text{(B6)}$$

and by substitution into Eq. (B4),

$$\hat{v}_f(Z_i) = -a\left[\frac{Z_i}{N_0\Gamma(7)}\right]^{b/7} \frac{\Gamma(7 + b)}{\Gamma(7)} \left[\frac{\rho_0}{\rho(z)}\right]^{0.4}. \quad \text{(B7)}$$

The density factor $[\rho_0/\rho(z)]^{0.4}$ accounts for the increased fallspeed of precipitation in less dense air (Foote and du Toit, 1969). This is the formulation used to determine $\hat{v}_f$ as discussed in the text.

REFERENCES

Atlas, D., R. C. Srivastava and R. S. Sekhon, 1973: Doppler radar characteristics of precipitation at vertical incidence. *Rev. Geophys. Space Phys.*, **11**, 1–35.

Battan, L. J., 1973: *Radar Observation of the Atmosphere.* University of Chicago Press, 324 pp.

Churchill, D. D., and R. A. Houze, Jr., 1984: Development and structure of winter monsoon cloud clusters on 10 December 1978. *J. Atmos. Sci.*, **41**, 933–960.

Foote, G. B., and P. S. du Toit, 1969: Terminal velocity of raindrops aloft. *J. Appl. Meteor.*, **8**, 249–253.

Gamache, J. F., and R. A. Houze, Jr., 1982: Mesoscale air motions associated with a tropical squall line. *Mon. Wea. Rev.*, **110**, 118–135.

——, and ——, 1983: Water budget of a mesoscale convective system in the tropics. *J. Atmos. Sci.*, **40**, 1835–1850.

Herzegh, P. H., and P. V. Hobbs, 1980: The mesoscale and microscale structure and organization of clouds and precipitation in midlatitude cyclones. II: Warm-frontal clouds. *J. Atmos. Sci.*, **37**, 597–611.

Hobbs, P. V., 1974: *Ice Physics.* Clarendon Press, 863 pp.

Houze, R. A., Jr., and E. N. Rappaport, 1984: Air motions and precipitation structure of an early summer squall line over the eastern tropical Atlantic. *J. Atmos. Sci.*, **41**, 553–574.

——, P. V. Hobbs, P. H. Herzegh and D. B. Parsons, 1979: Size distributions of precipitation particles in frontal clouds. *J. Atmos. Sci.*, **36**, 156–162.

Johnson, R. H., 1982: Vertical motion in near-equatorial winter monsoon convection. *J. Meteor. Soc. Japan*, **60**, 682–690.

Kessler, E., 1969: *On the Distribution and Continuity of Water Substance in Atmospheric Circulations. Meteor. Monogr.*, No. 32, Amer. Meteor. Soc., 83 pp.

Leary, C. A., and R. A. Houze, Jr., 1979: The structure and evolution of convection in a tropical cloud cluster. *J. Atmos. Sci.*, **36**, 437–457.

Locatelli, J. D., and P. V. Hobbs, 1974: Fallspeeds and masses of solid precipitation particles. *J. Geophys. Res.*, **79**, 2185–2197.

Rutledge, S. A., and P. V. Hobbs, 1983: The mesoscale and microscale structure and organization of clouds and precipitation in midlatitude cyclones. VIII: A model for the "seeder–feeder" process in warm-frontal rainbands. *J. Atmos. Sci.*, **40**, 1185–1206.